Grid Current Shaping Method with DC-Link Shunt Compensator for Three-Phase Diode Rectifier-Fed Motor Drive System

Hojoon Shin, *Student Member, IEEE*, Yeongrack Son, *Student Member, IEEE*, and Jung-Ik Ha, *Senior Member, IEEE*

***Abstract*—This paper proposes grid current shaping method using dc-link shunt compensator for three-phase diode rectifier system without electrolytic dc-link capacitor. In the proposed method, the diode rectifier system can satisfy the grid regulation IEC61000-3-12 without any power factor correction circuit or heavy grid filter inductor. The proposed grid current shaping method can be realized by applying DSC with reduced-rating components and without electrolytic capacitor, which is connected parallel to the dc link. Since DSC has no electrolytic capacitor, the system with DSC has high circuit reliability. Furthermore, DSC can enhance the system efficiency, especially in flux-weakening area, since the motor drive inverter recovers the reduced modulation index, which has been spent in the additional control for small passive components. This paper presents the control method for DSC and analyzes the effect of proposed method. The feasibility of proposed method is verified by simulation and experimental results.**

***Index Terms*—DC-link shunt compensator (DSC), electrolytic capacitor-less system, grid current harmonic improvement, motor drive inverter, three-phase diode rectifier system.**

I. Introduction

THE conventional diode rectifier-fed system shown in Fig. 1 applies passive components such as grid filter inductor and dc-link capacitor for smoothing the output power and reducing the grid current harmonics. However, these components occupy so much space so that the size of the overall system is dominantly determined by them. Furthermore, the electrolytic capacitor in dc link is prone to failure and severely lowers the reliability of the system. Therefore, many engineers have been investigated about the methods for reducing or removing the electrolytic capacitor [1]–[12]. Most of the alternative systems usually replace the electrolytic capacitor in dc link with film or ceramic capacitor, which has much higher reliability but much less capacitance per unit volume than the electrolytic one. These systems are named as "small dc-link capacitor system" or "reduced dc-link capacitor system" [13]–[15].

The small dc-link capacitor system (SDCS) has stability issue due to the reduced dc-link capacitance and negative impedance characteristic caused by constant power load (CPL). Several stabilization methods for the small dc-link capacitor system have been proposed to solve this problem [1]–[5], [8], [16]–[18]. These stabilization methods apply additional voltage to the motor to stabilize the system, so they can suffer the degradation of system performances, such as the torque fluctuation and the reduced efficiency. Other methods with auxiliary circuits which perform the stabilization control instead of the motor drive inverter have been also proposed to stabilize the system with enhanced motor drive performance [9]–[11], [19].

On the other hand, many researchers have found that SDCS basically also has low grid current harmonics as well as high reliability [13]–[15], since the small capacitance in dc link makes less effects on the grid current harmonics [21], [22]. As shown in Fig. 2 and Table I, the grid currents of SDCS without grid filter inductor satisfy the grid harmonic regulation of IEC61000-3-12

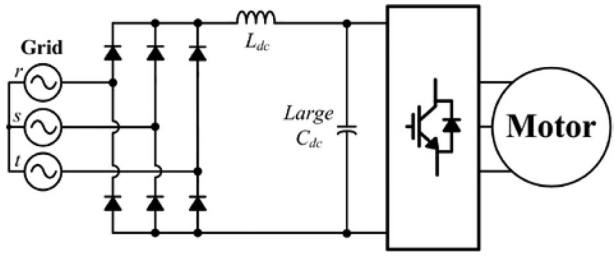

Fig. 1. Conventional three-phase diode rectifier system.

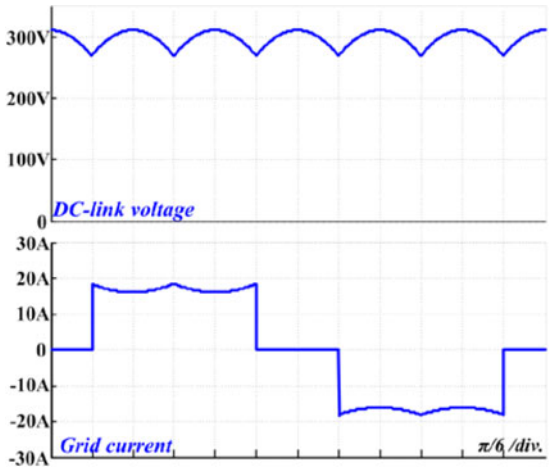

Fig. 2. DC-link voltage and grid current of three-phase SDCS without grid filter inductor.

Manuscript received August 24, 2015; revised December 29, 2015; accepted February 23, 2016. Date of publication March 10, 2016; date of current version November 11, 2016. Recommended for publication by Associate Editor V. Staudt.

H. Shin was with the Department of Electrical and Computer Engineering, Seoul National University, Seoul 08826, Korea. He is now with Hyundai Motor Company, Gyeonggi 18280, Korea (e-mail: nanshj@snu.ac.kr).

Y. Son and J.-I. Ha is with the Department of Electrical and Computer Engineering, Seoul National University, Seoul 08826, Korea (e-mail: syrident@snu.ac.kr; jungikha@snu.ac.kr).

Color versions of one or more of the figures in this paper are available online at http://ieeexplore.ieee.org.

Digital Object Identifier 10.1109/TPEL.2016.2540651

TABLE I
GRID CURRENT HARMONIC OF SDCS WITHOUT A GRID FILTER INDUCTOR

Odd-Order Harmonics, THD, and PWHD (I_n/I_1, %)						
	I_5	I_7	I_{11}	I_{13}	THD	PWHD
IEC61000-3-12, $R_{\mathrm{sce.min}} = 350$	40	25	15	10	48	45
SDCS w/o L_{dc}	17.59	17.00	9.12	8.80	30.25	*61.91*
Even-Order Harmonics (I_n/I_1, %)						
	I_2	I_4	I_6	I_8	I_{10}	I_{12}
IEC61000-3-12, $R_{\mathrm{sce.min}} = 350$	8	4	2.7	2	1.6	1.3
SDCS w/o L_{dc}	0.03	0.10	0.29	0.12	0.05	0.07

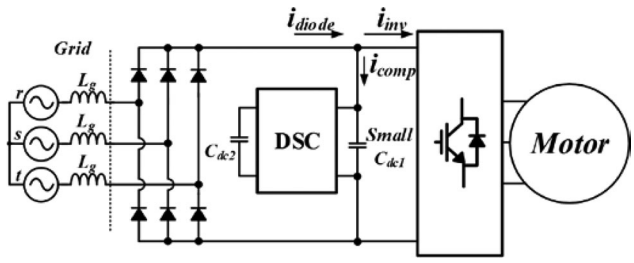

Fig. 3. Motor drive system with DSC.

$R_{\mathrm{sce.min}} = 350$" except partial weighted harmonic distortion (PWHD), which is defined as

$$\mathrm{PWHD} = \sqrt{\sum_{n=14}^{40} n \left(\frac{I_n}{I_1}\right)^2} \tag{1}$$

where I_1 is the magnitude of the fundamental grid current and I_n is the magnitude of the n-order harmonic current. It means that the system can satisfy the grid regulation and be applied to industry applications, such as air compressor and pump, if higher order harmonics of grid current are improved. If some current harmonics under the limits are granted, the compensation circuit can be miniaturized in comparison with other circuits, which synthesize sinusoidal grid current [23]–[26].

This paper proposes the grid current shaping method for SDCS with a dc-link shunt compensator (DSC) as in Fig. 3. By using a compensation current i_{comp} from the proposed method, DSC system (DSCS) can satisfy grid regulation IEC61000-3-12 without a heavy grid-side inductor. Since i_{comp} generated by DSC is made up of small amount of ripple power to attenuate higher order harmonics, DSC is designed with small rating components and can be miniaturized. Although auxiliary circuit DSC is added, the efficiency of total motor drive system can be improved in flux weakening area by saving extra MI margin which should be used for grid current shaping method if DSC is not utilized. Therefore, the torque-ripple-free and more efficient motor drive system can be realized by adopting DSC. The validity and feasibility of proposed system are verified by the simulation and experimental results.

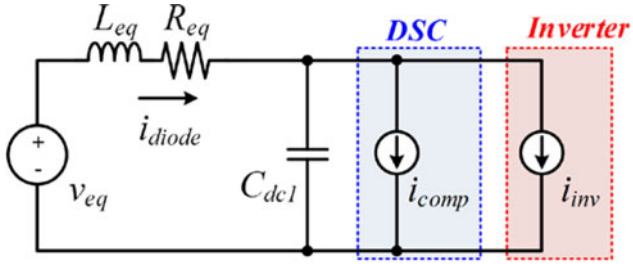

Fig. 4. Equivalent circuit, including i_{comp}.

II. GRID CURRENT SHAPING METHOD FOR A THREE-PHASE DIODE RECTIFIER-FED SYSTEM

From DSCS, an equivalent circuit including i_{comp} can be depicted as Fig. 4, where L_{eq} and R_{eq} are equivalent impedances represented as

$$\begin{aligned} R_{\mathrm{eq}} &= 2R_g + R_{\mathrm{dc}} + \frac{3\omega_g L_g}{\pi} \\ L_{\mathrm{eq}} &= 2L_g + L_{\mathrm{dc}} \end{aligned} \tag{2}$$

where L_g and R_g are the grid impedances, ω_g is the grid angular speed, and $3\omega_g L_g/p$ is a term for nonohmic voltage drop due to commutation [4], [5]. Since i_{comp} is injected from dc-link side, it is desirable that i_{comp} should be *6m* harmonics of grid angular frequency ($m = 1, 2, ...$) in order not to make unbalanced current into the three-phase grid. There are various candidates to meet this condition, and the waveform proportional to *6m* harmonics of dc-link voltage is one of the best solutions in terms of MI utilization and grid current harmonics reduction. At first, from Fig. 4, the inverter current i_{inv} can be derived as

$$i_{\mathrm{inv}} = \frac{P_{\mathrm{inv}}}{\nu_{\mathrm{dc1}}} = \frac{P_{\mathrm{inv}}}{V_{\mathrm{dc0}} + \tilde{\nu}_{\mathrm{dc1}}} \approx \frac{P_{\mathrm{inv}}}{V_{\mathrm{dc0}}} - \frac{P_{\mathrm{inv}}}{V_{\mathrm{dc0}}^2}\tilde{\nu}_{\mathrm{dc1}} \tag{3}$$

by Taylor series, where V_{dc0} is average value of main dc-link voltage, P_{inv} is amount of CPL, and $\tilde{\nu}_{\mathrm{dc1}}$ is *6m* harmonics in dc-link voltage. Referring to the ripple value of i_{inv}, i_{comp} can be generated as

$$i_{\mathrm{comp}} = \alpha \frac{P_{\mathrm{inv}}}{V_{\mathrm{dc0}}^2}\tilde{\nu}_{\mathrm{dc1}} \tag{4}$$

where α is weighting factor. Then i_{diode} is calculated as

$$i_{\mathrm{diode}} \approx i_{\mathrm{inv}} + i_{\mathrm{comp}} = \frac{P_{\mathrm{inv}}}{V_{\mathrm{dc0}}} + (\alpha - 1)\frac{P_{\mathrm{inv}}}{V_{\mathrm{dc0}}^2}\tilde{\nu}_{\mathrm{dc1}} \tag{5}$$

Here, it is assumed that dc-link capacitor current i_{dc} is negligible due to very small C_{dc}. i_{diode} becomes constant value $P_{\mathrm{inv}}/V_{\mathrm{dc0}}$ where α is 1. If α is higher than unity, however, the second term in the right side of (5) is increased and the harmonics of grid current are also changed. Since these added harmonics contain *6m* harmonics of grid angle and are even-function, they have equal influence on three-phase grid current. Furthermore, since i_{comp} is controlled as (4), harmonic influence on the grid side is theoretically maintained regardless of output power condition.

i_{diode} in (5) becomes each of three-phase grid currents when corresponding diodes are conducting. The waveform of one grid

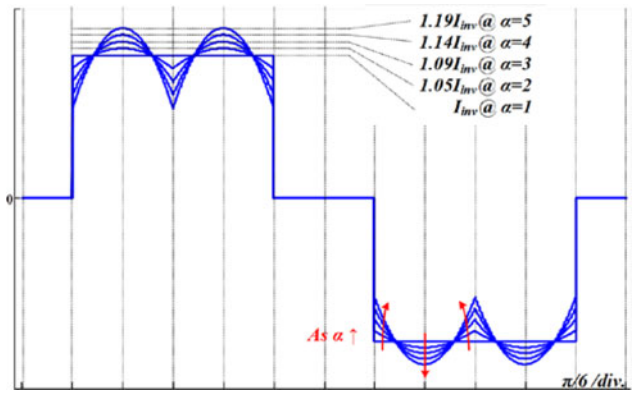

Fig. 5. Grid current shape variation according to α.

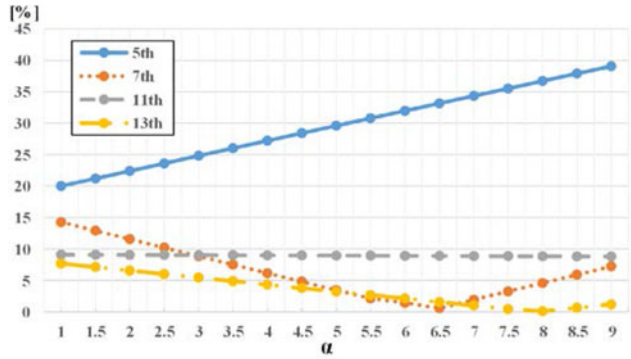

Fig. 6. Grid current odd-order harmonics variations according to α.

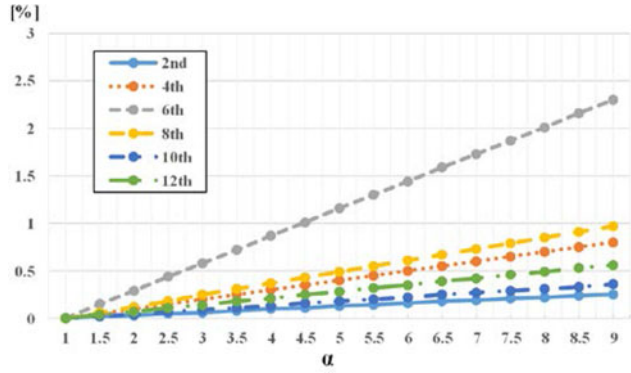

Fig. 7. Grid current even-order harmonics variations according to α.

current is shown in Fig. 5 in case that grid-side inductance is negligible. As shown in this figure, the shape of grid current is clear square wave where $\alpha = 1$, and the smooth waveform is obtained as α is increased.

Assuming that the system is stable and the grid voltage is $V_m \cdot cos(\omega_g t)$ where V_m is peak value of grid voltage and ω_g is grid angular speed, $\tilde{\nu}_{\mathrm{dc1}}$ becomes maximum value of line-to-line grid voltage and expressed as

$$\tilde{\nu}_{\mathrm{dc1}} \approx V_m \cos\left(\omega_g t - (2k-1)\frac{\pi}{6}\right) - V_{\mathrm{dc0}} \tag{6}$$

where $k = 1, 2, \ldots 6$ during one grid period. Here, V_m can be calculated as

$$V_m = \frac{\pi}{3} V_{\mathrm{dc0}} \tag{7}$$

by using that the average value of (6) is zero. From (5), i_{diode} can be derived as

$$\begin{aligned} i_{\mathrm{diode}} = \; & (2-\alpha)\frac{P_{\mathrm{inv}}}{V_{\mathrm{dc0}}} + (\alpha-1)\frac{\pi}{3}\frac{P_{\mathrm{inv}}}{V_{\mathrm{dc0}}} \\ & \times \cos\left(\omega_g t - (2k-1)\frac{\pi}{6}\right). \end{aligned} \tag{8}$$

The grid current i_g shown in Fig. 5 can be calculated from (8). The Fourier series form of i_g is shown as follows:

$$i_g = a_0 + \sum_{n=1}^{\infty} \left(a_n \cos(n\omega_g t) + b_n \sin(n\omega_g t)\right) \tag{9}$$

where a_0 and b_n are zero, and a_{n} is given by (10) shown at the bottom of the page. From (10) , magnitude of each harmonics $|i_g(n)|$ is rearranged to

$$|i_g(n)| = a_n = \left| \begin{array}{l} \dfrac{P_{\mathrm{inv}}}{V_{\mathrm{dc0}}}\left(2O(n) - \dfrac{\pi}{3}P(n)\right) \\ +\dfrac{P_{\mathrm{inv}}}{V_{\mathrm{dc0}}}\left(\dfrac{\pi}{3}P(n) - O(n)\right)\alpha \end{array} \right|. \tag{11}$$

Here, a_n is linearly decreasing as α is increasing from the most of harmonics except fifth- and even-order harmonics. By using this factor, grid current harmonics can be adjusted.

Figs. 6 and 7 show the odd- and even-order harmonics of the grid current, respectively, and Fig. 8 describes the total harmonic distortion (THD) and PWHD. As α is increased, most of odd-order harmonics are reduced except the fifth-order harmonic, whereas even-order harmonics shown in Fig. 7 are slightly increased. The increments of even-order harmonics are relatively very small in comparison with variations of odd-order

$$\begin{aligned} a_n = \; & (2-\alpha)\frac{P_{\mathrm{inv}}}{V_{\mathrm{dc0}}} \overbrace{\frac{2}{n\pi}\left(\sin\left(n\frac{\pi}{3}\right) + \sin\left(n\frac{2\pi}{3}\right)\right)}^{O(n)} \\ & + (\alpha-1)\frac{\pi}{3}\frac{P_{\mathrm{inv}}}{V_{\mathrm{dc0}}} \overbrace{\frac{1}{\pi}\left\{\begin{array}{l} \frac{1}{n-1}\left(\sin\left(\frac{\pi}{3}n - \frac{\pi}{6}\right) - \sin\frac{\pi}{6} - \sin\left(\pi n - \frac{\pi}{6}\right) + \sin\left(\frac{2\pi}{3}n + \frac{\pi}{6}\right)\right) \\ +\frac{1}{n+1}\left(\sin\left(\frac{\pi}{3}n + \frac{\pi}{6}\right) + \sin\frac{\pi}{6} - \sin\left(\pi n + \frac{\pi}{6}\right) + \sin\left(\frac{2\pi}{3}n - \frac{\pi}{6}\right)\right) \end{array}\right\}}^{P(n)} \end{aligned} \tag{10}$$

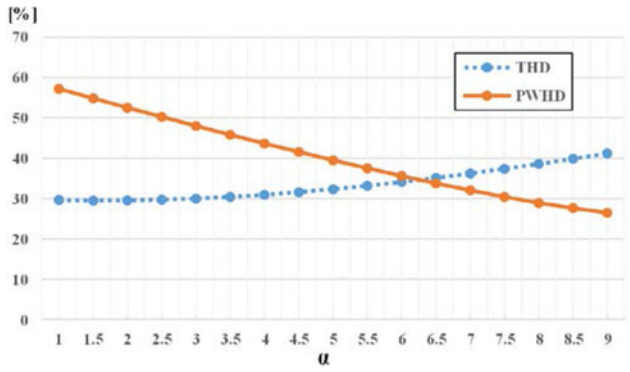

Fig. 8. Grid current THD and PWHD variations according to α.

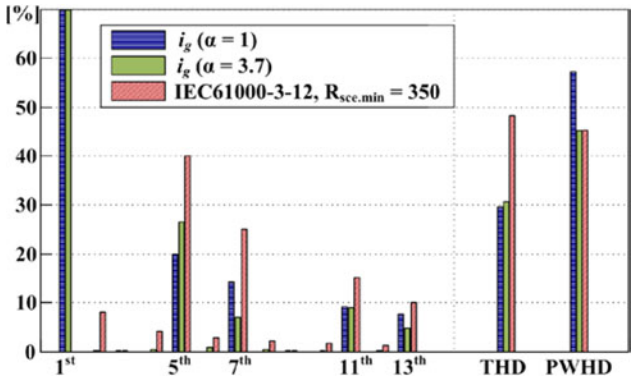

Fig. 9. Simulation results of grid current harmonics where $\alpha = 1$ and 3.7.

harmonics. The harmonics are increased again when their sign is reversed. The magnitudes of 7th and 13th-order harmonics rebound at $\alpha \geq 6.5$ and $\alpha \geq 8$, respectively, and the rebounded points of higher order harmonics are located at higher α. As shown in Fig. 8, the PWHD is steadily decreased since higher order harmonics over 14th are all decreased. By using this factor, the harmonics can be reduced below the limit by adjusting α.

For example, Fig. 9 shows the fast Fourier transform (FFT) results of the waveforms in comparison with grid regulation IEC61000-3-12 $R_{\mathrm{sce.min}} = 350$". In the case of square wave $(\alpha = 1)$, the harmonics of the waveform meets grid regulation except PWHD. However, in case that $\alpha > 1$, PWHD is gradually decreased and satisfies the grid regulation of 45% at $\alpha = 3.7$ (PWHD $= 44.96\%$). Although the fifth-order and even-order harmonics are increased, they still have enough margin to reach grid regulations. Therefore, the system with DSC can satisfy grid regulation where $\alpha > 3.7$. By adopting this proposed method, the system always provides same harmonic spectrum regardless of P_{inv} since compensation harmonics is proportional to P_{inv}.

III. DC-Link Shunt Compensator System

A. System Configuration

The configuration of the system including DSC is shown in Fig. 10. In comparison with the conventional diode rectifier system, the heavy dc reactor and the dc-link capacitor are

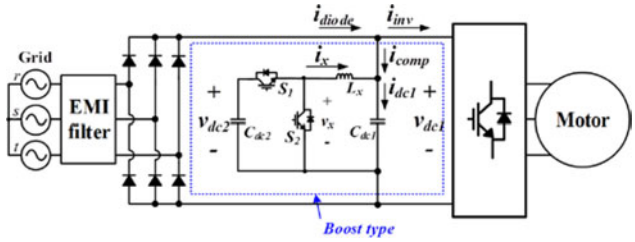

Fig. 10. Configuration of the system with boost-type DSC.

replaced with DSC. In this figure, DSC is implemented as boost converter, but it is also possible to adopt other converters that can transfer the power to floating capacitor C_{dc2}. There are two important considerations to decide type of DSC: One is energy capacity and another is system miniaturization. For example, in cases of boost and buck converters, their capable energy can be calculated by using capacitor energy capacity

$$E = \frac{1}{2} C_{\mathrm{dc2}} (V_{\mathrm{dc2.max}}^2 - V_{\mathrm{dc2.min}}^2) \tag{12}$$

where the maximum and minimum available capacitor voltages are, respectively, $V_{\mathrm{dc2.max}}$ and $V_{\mathrm{dc2.min}}$. In the former case, E is 28800 C_{dc2} J where $V_{\mathrm{dc2.max}}$ and $V_{\mathrm{dc2.min}}$ are set to 400 and 320 V, respectively, considering $220 - V_{\mathrm{rms}}$ system with a 600 V device. In contrast, E of the latter is $31250 C_{\mathrm{dc2}}$ J where $V_{\mathrm{dc2.max}}$ and $V_{\mathrm{dc2.min}}$ are 250 and 0 V, respectively. Therefore, the latter has slightly high energy capacity. However, the DSC characteristics such as efficiency and design factor are changed because inductor current of the latter is higher than that of the former assuming that the average output current is same. Moreover, the former has great advantage of continuous output current, which is important for the proposed control method. Thus, this paper chooses boost converter as a DSC structure.

The boost converter, which shares the ground with main system, also has many merits in low-cost system implementations such as gate power supply with bootstrap circuit, voltage sensing without photocoupler or isolation sensor, and inductor current sensing by using shunt resistor. In summary, it is desirable for adopting the boost converter as DSC, considering substantive circuit design.

B. Control of DSC

The control block diagram for DSC is described in Fig. 11. The blocks are divided into three parts: ν_{dc2} controller, grid current shaping block, and current controller. In ν_{dc2} controller, the average value of floating dc-link voltage ν_{dc2} is regulated as its reference value ν_{dc2}^*. PI controller is used for the regulator, and the floating capacitor current reference i_{dc2}^* is generated by summation of the voltage controller output $i_{\mathrm{dc2.fb}}$ and feedforward term $i_{\mathrm{dc2.ff}}$. The derivation of feedforward term will be explained in subsection *C*. Finally, the C_{dc2} current reference $i_{\nu c}^*$ is generated after passing a notch filter which is designed for removing ripples which come from ν_{dc2}. Since the main frequency of this ripple is $6\,\omega_g\,(\omega_g = 120\pi\ rad/s)$, the bandwidth of notch filter ω_{NF} is designed as 720π rad/s and damping ration ζ_{NF} is set to 0.707.

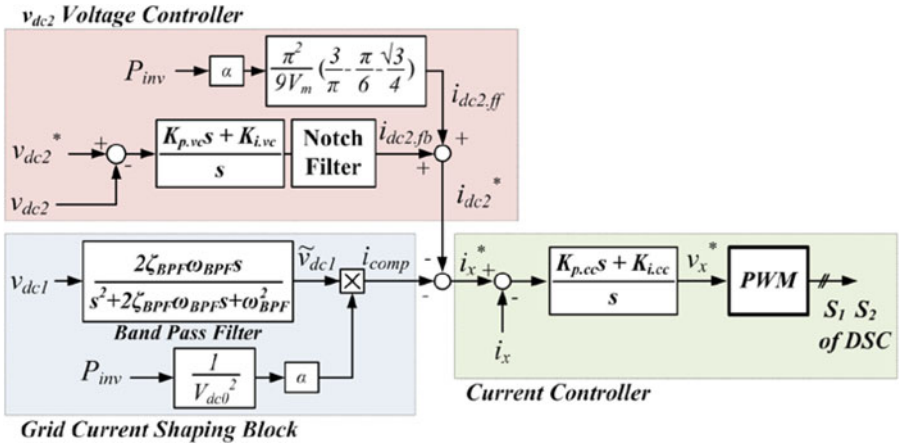

Fig. 11. Control block diagram of DSC.

To design two gains of voltage controller, $K_{i.\nu c}$ and $K_{p.\nu c}$, the transfer function of voltage controller can be derived as (13). Here, the notch filter is neglected considering that the bandwidth of voltage controller $\omega_{\nu c}$ is much smaller than $\omega_{\rm NF}$. Therefore, the transfer function of the notch filter can be assumed unity near $\omega_{\nu c}$

$$\frac{\nu_{\rm dc2}}{\nu_{\rm dc2}^*}=\frac{(K_{p.\nu c}/C_{\rm dc2})s+(K_{i.\nu c}/C_{\rm dc2})}{s^2+(K_{p.\nu c}/C_{\rm dc2})s+(K_{i.\nu c}/C_{\rm dc2})}. \tag{13}$$

Comparing with the general form of second order transfer function represented as

$$\frac{\nu_{\rm dc2}}{\nu_{\rm dc2}^*}=\frac{2\zeta_{\nu c}\omega_{\nu c}s+\omega_{\nu c}^2}{s^2+2\zeta_{\nu c}\omega_{\nu c}s+\omega_{\nu c}^2}. \tag{14}$$

$K_{p.\nu c}$ and $K_{i.\nu c}$ are set to

$$K_{p.\nu c}=2C_{dc2}\zeta_{\nu c}\omega_{\nu c}\ \text{ and }\ K_{i.\nu c}=C_{\rm dc2}\omega_{\nu c}^2 \tag{15}$$

respectively. In this paper, $\omega_{\nu c}$ is set to 20π rad/s. From (13), if $\zeta_{\nu c}$ is too small, the transfer function shows overshoot near $\omega_{\nu c}$. Therefore, it is good to set $\zeta_{\nu c}$, high enough for mitigating the overshoot, and it is recommended that $\zeta_{\nu c}$ is designed as around 3–5.

In the grid current shaping block, $\tilde{\nu}_{\rm dc1}$ is generated by band-pass filter (BPF), which has a wide bandwidth to extract *6m* harmonics in $\nu_{\rm dc1}$. Here, the bandwidth $\omega_{\rm BPF}$ and damping ratio of BPF $\zeta_{\rm BPF}$ are set to 720π rad/s and 5, respectively. By using this extracted harmonics and (4), $i_{\rm comp}$ can be easily obtained. Then the sum of $i_{\rm comp}$ and $i_{\rm dc2}^*$ becomes the current reference i_x^*, which is the input of current controller. The PI controller is also used for the current controller, and the two gains $K_{p.\rm cc}$ and $K_{i.\rm cc}$ are set to

$$K_{p.\rm cc}=L_x\omega_{\rm cc}\quad\text{and}\quad K_{i.\rm cc}=R_x\omega_{\rm cc} \tag{16}$$

respectively, where L_x is the inductor, R_x is the ESR of L_x, and $\omega_{\rm cc}$ is the bandwidth of the current controller. Then the transfer function of this controller can be simplified as

$$\frac{i_x}{i_x^*}=\frac{sK_{p.\rm cc}+K_{i.\rm cc}}{s^2L_x+s(K_{p.\rm cc}+R_x)+K_{i.\rm cc}}=\frac{\omega_{\rm cc}}{s+\omega_{\rm cc}}. \tag{17}$$

It is desired to design $\omega_{\rm cc}$ as high as possible, because i_x^* contains *6 m* harmonics of ω_g. However, the switching frequency of DSC should be also considered when we design $\omega_{\rm cc}$.

The dynamic response of the proposed method can be easily demonstrated. The proposed method is based on current injection, and the compensation current $i_{\rm comp}$ is generated by using the load power $P_{\rm inv}$, as shown in (4). Here, assuming that $i_{\rm dc2}^*$ can be neglected, current reference i_x^* equals to $i_{\rm comp}$ and it means that i_x^* is proportional to $P_{\rm inv}$. By using the transfer function of DSC current control loop shown in (17), L_x current i_x can be expressed as

$$i_x=\frac{\omega_{\rm cc}}{s+\omega_{\rm cc}}i_x^*\approx\frac{\omega_{\rm cc}}{s+\omega_{\rm cc}}\alpha\frac{\tilde{\nu}_{\rm dc1}}{V_{\rm dc0}^2}P_{\rm inv}. \tag{18}$$

From this equation, i_x shows the response characteristic of first-order low-pass filter where $P_{\rm inv}$ is changed. The response time is totally decided by the bandwidth of current controller $\omega_{\rm cc}$. Therefore, it is advantageous to gain $\omega_{\rm cc}$ as high as possible in terms of the dynamic response of the proposed method.

C. System Parameters Design

1) $C_{\rm dc2}$ Design: In the DSCS, the role of $C_{\rm dc2}$ is to absorb the ripple corresponding to (12), and the capacitance should be designed considering a variation of $\nu_{\rm dc2}$ caused by the ripple. A maximum available voltage $V_{\rm dc2.max}$ is commonly decided by the voltage rating of used components such as the switching device or capacitor, and a minimum voltage limitation $V_{\rm dc2.min}$ is decided as a value higher than $\nu_{\rm dc1}$. The minimum limitation is related to the duty margin of boost type DSC, in other words, the duty of DSC should be maintained under the unity. For example, in the case of $220-V_{\rm rms}$ three-phase grid tied system, 600-V switching devices are used, and $\nu_{\rm dc1}$ is maximum value of line-to-line voltage and its peak value is 311 V. Then the $V_{\rm dc2.max}$ is set to 400 V considering safety level against voltage spiking from each switching device, and $V_{\rm dc2.min}$ is chosen as 320 V considering voltage ripples in $\nu_{\rm dc1}$ owing to the switching current.

Assuming that i_x is well regulated to its reference, the capacitor energy equation from $C_{\rm dc2}$ is

$$\frac{1}{2}C_{\rm dc2}\nu_{\rm dc2}^2 = \int(-\nu_x i_x)dt + C \tag{19}$$

where ν_x is an average leg output voltage as shown in Fig. 10 and C is integral coefficient. Assuming that equivalent series resistance (ESR) of L_x is neglected, ν_x is derived as

$$\nu_x = L_x\frac{di_x}{dt} + \nu_{\rm dc1}. \tag{20}$$

By substituting (4) and (20) into (19), $\nu_{\rm dc2}$ is calculated in (21) during $-\pi/6 < \omega_g t < \pi/6$. Here, $\nu_{\rm dc1}$ is assumed as $V_m cos(\omega_g t)$ for the convenient calculation. In (21), $i_{\rm dc2}$ is not neglected because it is necessary to maintain balance of capacitor energy from (19). By using that $\nu_{\rm dc2}(-\pi/(6\omega_g))$ and $\nu_{\rm dc2}(\pi/(6\omega_g))$ should be same, $i_{\rm dc2}$ is expressed as (20) at bottom of the page.

$$i_{\rm dc2} = \frac{\alpha\pi^2 P_{\rm inv}}{9V_m}\left(\frac{3}{\pi} - \frac{\pi}{6} - \frac{\sqrt{3}}{4}\right) \equiv i_{\rm dc2.ff}. \tag{22}$$

For example, $i_{\rm dc2}$ is -0.13 A where $P_{\rm inv} = 5.5$ kW, $V_m = 311$V, and $\alpha = 4$. This value is negligible in comparison with $i_{\rm comp}$, but it keeps energy of $C_{\rm dc2}$ be balanced. Since $i_{\rm dc2}$ is covered by a voltage controller in Fig. 10, the value in (22) is used for feedforward of this controller. From (21), C is calculated as (23) by using that the average value of $\nu_{\rm dc2}$ is $\nu_{\rm dc2}^*$

$$C = \frac{C_{\rm dc2}\nu_{\rm dc2}^{*2}}{2} - \left(\frac{\alpha^2\pi^4 L_x P_{\rm inv}^2}{324V_m^2}\left(\frac{\pi}{\sqrt{3}} + 1\right)\right). \tag{23}$$

Fig. 12 shows $\nu_{\rm dc2}$ in accordance with various $C_{\rm dc2}$. From (21), the peak value of $\nu_{\rm dc2}$ becomes 400 V where $C_{\rm dc2}$ is around 38 μF. Therefore, $\nu_{\rm dc2}$ is bounded between $V_{\rm dc2.max}$ and $V_{\rm dc2.min}$ where $C_{\rm dc2} \geq 38$ μF. Based on $C_{\rm dc2}$ and (12), power rating of DSC less than 10% of rated power of the main system, about 6% and 7.2% if 50 and 60 Hz systems are considered, respectively. The duty of DSC D_x expressed in (24) is also illustrated in Fig. 12

$$D_x = \frac{\nu_x}{\nu_{\rm dc2}}. \tag{24}$$

In the case that $C_{\rm dc2} > 38$ μF, since $\nu_{\rm dc2}$ is always higher than $\nu_{\rm dc1}$, it is guaranteed that D_x does not exceed unity.

2) L_x and $C_{\rm dc1}$ Design: L_x from DSCS is related with current synthesis and switching ripple current of i_x. Since i_x is varied sharply and the basic concept of proposed control is current injection, it is advantageous to choose high switching frequency $f_{\rm sw\cdot DSC}$. By using inductor voltage equation at boost converter turn-on state, the value of L_x is calculated as

$$L_x = \frac{(\nu_{\rm dc2} - \nu_{\rm dc1})T_{\rm sw}D_x}{\Delta i_x} \tag{25}$$

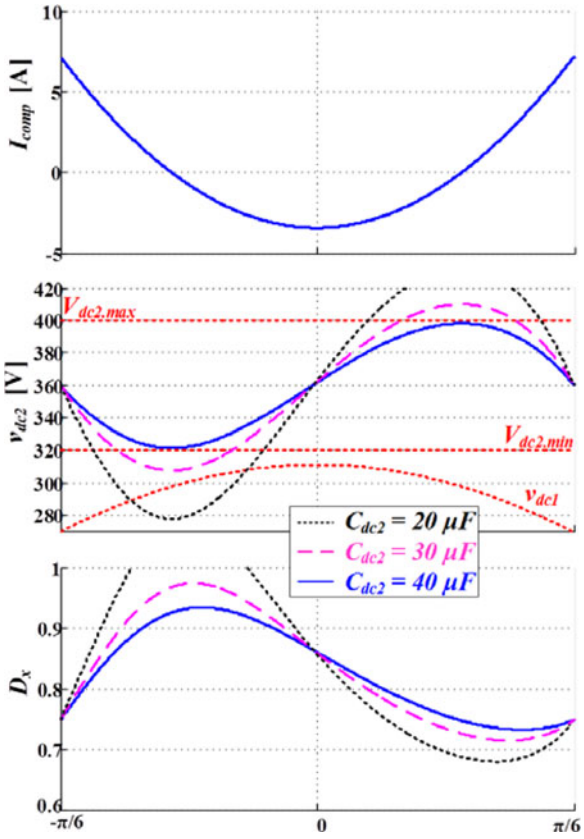

Fig. 12. $\nu_{\rm dc2}$ variation in accordance with various $C_{\rm dc2}$ where $P_{\rm inv} = 5.5$ kW, $\nu_{\rm dc2}^* = 360$ V, and $\alpha = 4$.

where Δi_x is switching ripple of i_x. In this paper, $f_{\rm sw.DSC}$ is 20 kHz considering the maximum switching frequency of IGBT, and the Δi_x is chosen as 4 A in order that peak value of $(i_x + 0.5\Delta i_x)$ should not exceed 10 A. And then L_x becomes 0.9 mH.

$C_{\rm dc1}$ in the DSCS plays a role of switching ripple absorbing filter. The switching ripples come from both motor drive circuit and DSC, but the ripple from motor drive circuit is normally much higher than that from DSC. $C_{\rm dc1}$ is usually chosen sufficient value in order that the peak value of $\nu_{\rm dc1}$ does not exceed $V_{\rm dc2.min}$. However, if the value of $C_{\rm dc1}$ is too high, it has bad influence on grid current harmonic. In this paper, $C_{\rm dc1}$ is chosen as 20 μF.

IV. Experimental Results

The experiment with 220-$V_{\rm rms}$ 5.5-kW laboratory prototype motor drive system was performed. The system conditions are shown in Table II. TMS320F28335 was used for digital signal processor and the interior permanent magnet synchronous motor (IPMSM) for air compressor was tested. In this experiment, the

$$\nu_{\rm dc2} = \sqrt{\frac{2}{C_{\rm dc2}}\left\{\alpha\frac{\pi^2 P_{\rm inv}}{9}\left(\begin{array}{c}\frac{1}{2}t + \frac{1}{4\omega_g}\sin 2\omega_g t - \frac{\alpha L_x \pi^2 P_{\rm inv}}{36V_m^2}\cos 2\omega_g t \\ + \frac{\alpha L_x \pi P_{\rm inv}}{3V_m^2}\cos\omega_g t - \frac{3}{\pi\omega_g}\sin\omega_g t\end{array}\right) - i_{\rm dc2}\left(\frac{\alpha L_x \pi^2 P_{\rm inv}}{9V_m}\cos\omega_g t - \frac{V_m}{\omega_g}\sin\omega_g t\right)\right\} + \frac{2C}{C_{\rm dc2}}} \tag{21}$$

TABLE II
SYSTEM CONDITIONS AND PARAMETERS

Condition	Value
Grid voltage	$220V_{\mathrm{rms}}$
Grid angular frequency ω_g	377 rad/s
Inverter switching frequency $f_{\mathrm{sw}}.\mathrm{inv}$	10 kHz
DSC switching frequency $f_{\mathrm{sw.DSC}}$	20 kHz
Motor parameter	
Rated power P_{rated}	5500 W
Maximum speed $\omega_{\mathrm{rpm.max}}$	6000 r/min
d-Axis inductance L_d	2.16 mH
q-Axis inductance L_q	3.12 mH
Phase resistance R_s	0.1Ω
Flux linkage λ_{pm}	0.110 V·s/rad
Pole P	6

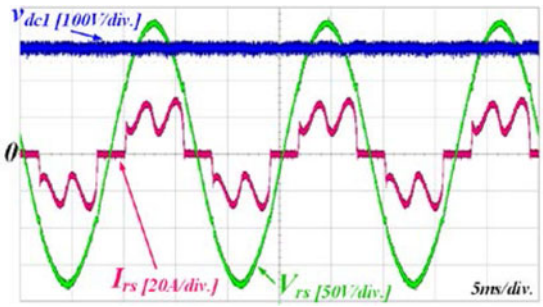

Fig. 13. Experimental results of conventional HPCS ($C_{\mathrm{dc}} = 2$ mF, $L_{\mathrm{dc}} = 0.7$ mH, $P_{\mathrm{inv}} = 5.5$ kW).

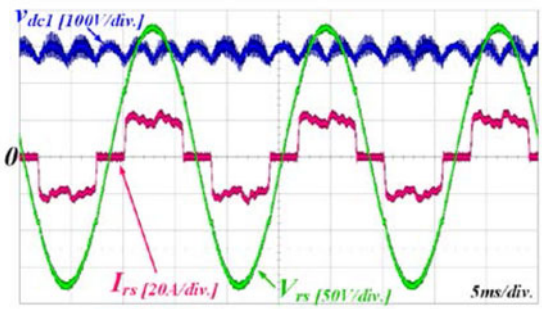

Fig. 14. Experimental results of SDCS with dc-link voltage stabilization control ($C_{\mathrm{dc}} = 20$ μF, $L_{\mathrm{dc}} = 0.7$ mH, $P_{\mathrm{inv}} = 5.5$ kW).

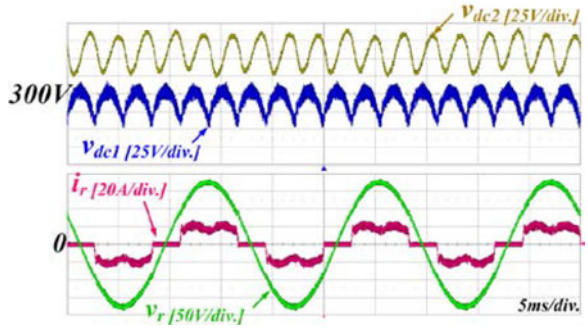

Fig. 15. Experimental results of DSCS: ν_{dc2}, ν_{dc1}, ν_{rs}, and i_{rs} where $P_{\mathrm{inv}} = 5.5$ kW, $\alpha = 4$.

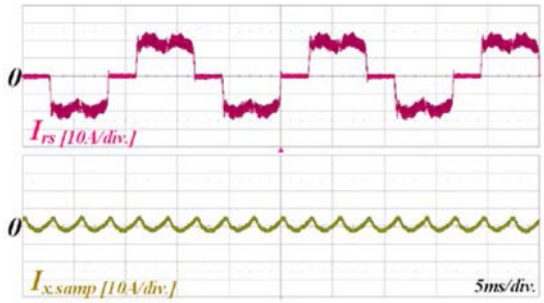

Fig. 16. Experimental results of DSCS: i_{rs} and i_x where $P_{\mathrm{inv}} = 5.5$ kW, $\alpha = 4$.

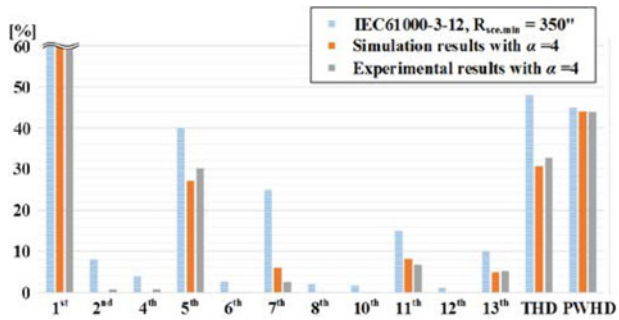

Fig. 17. Experimental results of DSCS: grid current harmonics where $P_{\mathrm{inv}} = 5.5$ kW.

performance of the three systems are compared: conventional heavy passive components system (HPCS), SDCS in [3], and the proposed DSCS. Electromagnetic interference (EMI) filter was adopted in all systems.

Fig. 13 shows experimental results of the conventional HPCS where the C_{dc} is 2.2 mF and the value of a dc reactor L_{dc} is 0.7 mH. The r-phase grid currents i_{rs} have values of $29A_{\mathrm{peak}}$ and $16A_{\mathrm{rms}}$, and they satisfy the grid regulation IEC61000-3-12. Due to the voltage drop of dc reactor, the average dc-link voltage is 295 V.

Fig. 14 exhibits experimental waveforms of SDCS where the capacitance is 20 μF. The grid regulation is satisfied with reduced passive components, but the motor side output performances are inevitably degraded due to the stabilization control in [3].

In the case of the proposed DSCS, two switching devices of 600 V and 14 A, an inductor L_x, which has value of 0.9 mH with greatly reduced current rating, and two capacitors (20 μF, 47 μF) are used. Figs. 15–17 show the experimental results of DSCS where $P_{\mathrm{inv}} = 5.5$ kW and $\alpha = 4$. In Fig. 15, r-phase grid current i_{rs} is smoothly controlled as desired value shown in Fig. 5, and it has the values of 24 A_{peak} and $16\mathrm{A}_{\mathrm{rms}}$. ν_{dc1} is regulated as the maximum of line-to-line grid voltages without unstable oscillation, and ν_{dc2}, which absorbs the ripple energy, is sufficiently bounded into the range from $V_{\mathrm{dc2.min}}$ (320 V) to $V_{\mathrm{dc2.max}}$ (400 V). The sampled inductor current $i_{x.\mathrm{samp}}$ and i_{rs} are compared in Fig. 16. $i_{x.\mathrm{samp}}$ has values of 8 A_{peak} and

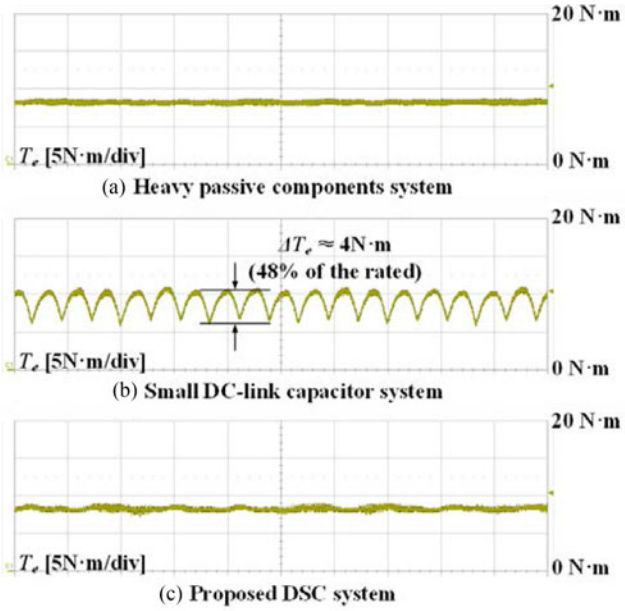

Fig. 18. Experimental results: ouput toques of (a) HPCS, (b) SDCS, and (c) DSCS where $P_{\rm inv} = 5.5$ kW.

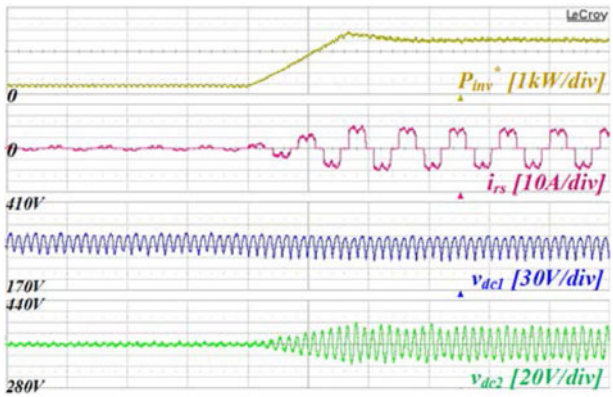

Fig. 19. Experimental results of DSCS: $i_{\rm rs}$, $\nu_{\rm dc}$, and $\nu_{\rm dc2}$ where $P_{\rm inv}$ is changed from 0.2 to 1 p.u.

3.4 $A_{\rm rms}$. Since i_x is much lower than $i_{\rm rs}$, L_x can be more lightly designed in comparison with $L_{\rm dc}$ in the conventional systems. Fig. 17 shows the grid current harmonics of DSCS. It was verified that the PWHD becomes lower than the limit and the system satisfies all grid regulations where $\alpha = 4$.

The output torque of SDCS shown in Fig. 18(b) shows 24.1% increased peak value ($T_{e.\rm peak} = 10.3$ Nm) and contains 48% ripple ($\Delta T_e = 4$ Nm) per rated torque, while those of other systems show constant value (8.3 N·m). Fig 19 shows waveforms of DSCS where $P_{\rm inv}$ is changed from 0.2 to 1 p.u. (1.1 to 5.5 kW) considering load change of air compressor. During transient time, $i_{\rm rs}$ and $\nu_{\rm dc2}$ show good performance without any overshoot as explained in Section III-B.

Finally, efficiencies of the systems are measured and compared with one another. The measuring points are 100%, 80%, 60%, 40%, 20%, and 10% of the rated power, and the output power is set to be proportional to square of motor speed. First,

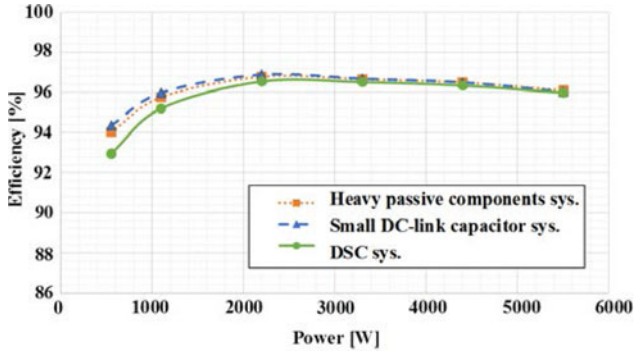

Fig. 20. Efficiencies of power conversion circuits.

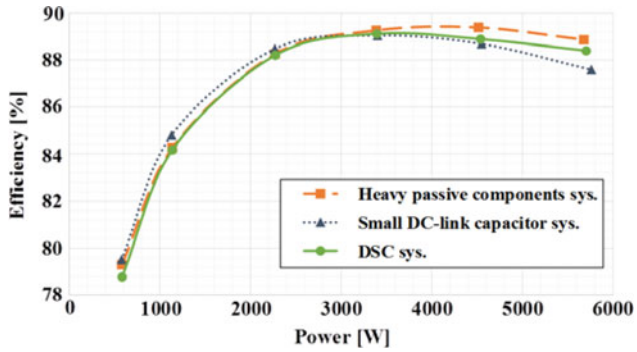

Fig. 21. System efficiencies including motor losses.

the efficiencies of the power conversion circuits except motor loss are compared as in Fig. 20. As shown in the figure, SDCS, which has a low dc-link voltage and low switching losses, shows the best efficiency. The proposed DSCS also has a similar dc-link voltage waveform, but its efficiency is slightly dropped due to the additional losses from DSC. At high-power area, since the conduction loss of $L_{\rm dc}$ is large, the efficiency difference between DSCS and other systems is smaller than at low-power area.

Next, efficiencies, including motor loss, are measured by using output of a dynamo. Though the losses of a dynamo are included, they are evenly included in all cases: thus, the tendency of efficiency curves are expected to be same. Fig. 21 shows the efficiencies of three systems. Before flux-weakening control area, three systems have almost same motor losses; thus, the efficiency depends on the losses of power conversion circuit. DSCS shows the lowest efficiency in low-power area due to the switching loss of DSC, but it is not major concern in the air compressor because the system quickly passes this area during acceleration. At flux-weakening control area, efficiencies of the systems are determined by amount of the output voltage margin. Since SDCS and DSCS have relatively low $\nu_{\rm dc1}$ (minimum $\nu_{\rm dc1}$ is around 260 V) and it makes the systems enter the flux weakening area earlier than HPCS, the efficiency of HPCS is highest. SDCS needs additional voltage margin for stabilization control, so it has the worst efficiency. In the case of DSCS, motor drive circuit in DSCS does not need the extra voltage margin due to the support of DSC. These factors save the *d*-axis current and

TABLE III
SYSTEM COMPARISON WITH THE CONVENTIONAL DIODE RECTIFIER-FED SYSTEMS

	Switch	DC Inductor	Capacitor
HPCS	–	0.7 mH, 360 Hz, 16 A_{rms}	680 μF × 4
SDCS	–	0.7 mH, 360 Hz, 16 A_{rms}	20 μF
DSCS	2	0.9 mH, 20 kHz, 3.4 A_{rms}	20 μF, 47 μF

TABLE IV
COST AND VOLUME COMPARISON

	Value	Part No.	Quantity	Unit Price ($)	Price ($)	Vol. (cm^3)
Proposed DSCS						
C_{dc1}	4.7 μF/450 V	ECW-FD2W475J	4	1.23	4.92	25.34
C_{dc2}	40 μF/450 V	B32776G4406K	1	14.99	14.99	43.51
S_1, S_2	14 A/600 V	STGPL6NC60D	2	0.78	1.56	1.68
Total cost					21.47 $	
Total volume					70.53 cm^3	
HPCS						
C_{dc}	680 μF/400 V	LLG2G681MELB45	4	6.69	26.76	132.82
	0.1 μF/450 V	ECW-FD2W104JQ	1	0.48	0.48	0.79
Total cost					27.24 $	
Total volume					133.61 cm^3	

DSCS can reduce motor copper loss in comparison with SDCS. Where output power is 5.5 kW, the efficiencies of three systems (HPCS, SDCS, and DSCS) are 88.87%, 87.59%, and 88.4%, respectively.

V. DISCUSSION

In this section, the practicability of the proposed DSCS in terms of the cost, size, reliability, and EMI characteristic in comparison with HPCS and SDCS will be discussed.

First, the benefits of the proposed DSCS in terms of the cost and size are discussed. The components used in HPCS, SDCS, and DSCS are listed as in Table III. Cost and volume of the systems are calculated as in Table IV. Here, cost of the component is based on the unit price of the online market and the volume information is from the value stated in the datasheet. As shown in the table, it can be found that the proposed DSCS has lower cost and volume than HPCS. The inductors used in the systems are not commercial products, so their cost and size cannot be clearly compared with one another. However, since the current rating of L_x is under 1/4 of the L_{dc} and the soft magnetic material core can be used in L_x instead of standard Si steel, the cost and size of DSCS, including the inductor, is expected to be advantageous than the conventional systems. Moreover, if MOSFETs are used in DSC instead of IGBTs, higher switching frequency can be achieved [9], [10]. This would have allowed to reduce L_x and increase ω_{cc}. It is possible since the DSC power being processes is small. Here, increased switching losses should be concerned.

Next, reliability of the proposed system compared to the conventional systems is discussed. Among many requirements for dc-link capacitor, ripple current capability is one of the most important characteristics. Unfortunately, the ripple current capability of electrolytic capacitor is limited as low value for preventing rapid evaporation of internal electrolyte; thus, many electrolytic capacitors should be used in order to satisfy ripple current rating [21]. On the contrary, film capacitor shows outstanding performance so that even one film capacitor can cover them in terms of ripple current capability. Even though some components for DSC are added in the proposed system, they have small power rating and are compact enough in comparison with the conventional bulky capacitor bank. Their reliability is surely higher than the conventional one considering the substantially used components. Furthermore, the proposed system has structural merit by reducing heavy gird filter inductor through the proposed grid current shaping method. The proposed method can be realized by simple control block; thus, the complexity of the proposed method is affordable.

Finally, the issue about the EMI filter is discussed. In the studies, which introduce a similar concept with DSC, it was proven that motor drive system impedance seen at the EMI filter is improved if we compensate a certain power proportional to the ripple of the dc-link voltage [3]–[6], [9]–[11]. So it is expected that there is no problem to adopt conventional EMI filter to the proposed DSC system [27]. Here, since switching of the additional switches in DSC makes high frequency noise, the noise in the grid is typically seen to increase if the system impedance is high. For this reason, parameters of the conventional EMI filter may be attenuated to suppress additional noise. However, it is expected that the EMI filter redesigning does not harm the advantages of the proposed DSC system in terms of cost and size.

VI. CONCLUSION

The grid current shaping method and DSC for three-phase system have been presented in this paper. By removing the electrolytic capacitor and grid filter inductor, the motor drive system with DSC fulfills robustness against component failure and circuit compactness. The grid current shaping method is proposed to cover the absence of the grid filter inductor, and the system satisfies grid current harmonics for the grid regulation, IEC61000-3-12 $R_{sce.min} = 350$" where $\alpha > 3.7$. Even though two switching devices are added, the size of inductor can be greatly reduced since the rated inductor current is decreased to about 79%, and the power rating of DSC can be designed as less than 10% of rated power of main system. The control method for the DSC system has been introduced, and the design guideline of floating capacitor, which is used for ripple energy storage, is proposed. In the experimental results, even though DSC is added, the system efficiency is improved at flux weakening area in comparison with conventional small dc-link capacitor system. The load power of air compressor is approximately proportional to square of motor speed and the system is mostly operated in flux-weakening area. Therefore, the efficiency in this operating area is an important factor to reduce energy consumption (in watt-hour). Therefore, it is verified that the proposed DSC system is a useful solution for small dc-link capacitor system.

REFERENCES

[1] Y. A.-R. I. Mohamed, A. A. A. Radwan, and T. K. Lee, "Decoupled reference-voltage-based active dc-link stabilization for PMSM drives with tight-speed regulation," *IEEE Trans. Ind. Electron.*, vol. 59, no. 12, pp. 4523–4536, Dec. 2012.

[2] A. Yoo, S.-K. Sul, H. Kim, and K.-S. Kim, "Flux-weakening strategy of an induction machine driven by an electrolytic-capacitor-less inverter," *IEEE Trans. Ind. Appl.*, vol. 47, no. 3, pp. 1328–1336, May/Jun. 2011.

[3] W.-J. Lee and S.-K. Sul, "DC-link voltage stabilization for reduced DC-link capacitor inverter," *IEEE Trans. Ind. Appl.*, vol. 50, no. 1, pp. 404–414, Jan.–Feb. 2014.

[4] R. Maheshwari, S. M. Nielsen, and K. Lu, "An active damping technique for small DC-link capacitor based drive system," *IEEE Trans. Ind. Informat.*, vol. 9, no. 2, pp. 848–858, May 2013.

[5] M. Hinkkanen and J. Luomi, "Induction motor drives equipped with diode rectifier and small DC-link capacitance," *IEEE Trans. Ind. Electron.*, vol. 55, no. 1, pp. 312–320, Jan. 2008.

[6] H. Wang and F. Blaabjerg, "Reliability of capacitors for DC-link applications in power electronic converters—An overview," *IEEE Trans. Ind. Appl.*, vol. 50, no. 5, pp. 3569–3578, Sep./Oct 2014.

[7] J. M. Galvez and M. Ordonez, "Swinging bus operation of inverters for fuel cell applications with small DC-link capacitance," *IEEE Trans. Power Electron.*, vol. 30, no. 2, pp. 1064–1075, Feb. 2015.

[8] M. Anun, M. Ordonez, I. G. Zurbriggen, and G. G. Oggier, "Circular switching surface technique: High-performance constant power load stabilization for electric vehicle systems," *IEEE Trans. Power Electron.*, vol. 30, no. 8, pp. 4560–4572, Aug. 2015.

[9] X. Zhang, X. Ruan, H. Kim, and C. K. Tse, "Adaptive active capacitor converter for improving stability of cascaded DC power supply system," *IEEE Trans. Power Electron.*, vol. 28, no. 4, pp. 1807–1816, Apr. 2013.

[10] H. Wang, H. S.-H. Chung, and W. Liu, "Use of a series voltage compensator for reduction of the DC-link capacitance in a capacitor-supported system," *IEEE Trans. Power Electron.*, vol. 29, no. 3, pp. 1163–1175, Mar. 2014.

[11] Q.-C. Zhong and Y. Zeng, "Control of inverter via a virtual capacitor to achieve capacitive output impedance," *IEEE Trans. Power Electron.*, vol. 29, no. 10, pp. 5568–5578, Oct. 2014.

[12] H. Ertl and J. W. Kolar, "A constant output current three-phase diode bridge rectifier employing a novel "electronic smoothing inductor," *IEEE Trans. Ind. Electron.*, vol. 52, no. 2, pp. 454–461, Apr. 2005.

[13] Y. Son and J-.I. Ha, "Direct power control of three phase inverter for grid input current shaping of single phase diode rectifier with small DC link capacitor," *IEEE Trans. Power Electron.*, vol. 30, no. 7, pp. 3794–3803, Jul. 2015.

[14] H.-S. Jung, S.-J. Chee, S.-K. Sul, Y.-J. Park, H.-S. Park, and W.-K. Kim, "Control of three-phase inverter for AC motor drive with small DC-link capacitor fed by single-phase AC source," *IEEE Trans. Ind. Appl.*, vol. 50, no. 2, pp. 1074–1081, Mar.–Apr. 2014.

[15] W.-J. Lee, Y. Son, and J.-I. Ha, "Single-phase active power filtering method using diode-rectifier-fed motor drive," *IEEE Trans. Ind. Appl.*, vol. 51, no. 3, pp. 2227–2236, May/Jun. 2015.

[16] H. Mosskull, "Optimal DC-link stabilization design," *IEEE Trans. Ind. Electron.*, vol. 62, no. 8, pp. 5031–5044, Aug. 2015.

[17] X. Liu, A. J. Forsyth, and A. M. Cross, "Negative input-resistance compensator for a constant power load," *IEEE Trans. Ind. Electron.*, vol. 54, no. 6, pp. 3188–3196, Dec. 2007.

[18] H. Mosskull, J. Galic, and B. Wahlberg, "Stabilization of induction motor drives with poorly damped input filters," *IEEE Trans. Ind. Electron.*, vol. 54, no. 5, pp. 2724–2734, Oct. 2007.

[19] H. Haga, "Power converter and its control method and air conditioner," U.S. Patent 8 269 370, Sep. 18, 2012.

[20] P. J. Grbovic, P. Delarue, and P. L. Moigne, "A novel three-phase diode boost rectifier using hybrid half-DC-bus-voltage rated boost converter," *IEEE Trans. Ind. Electron.*, vol. 58, no. 4, pp. 1316–1329, Apr. 2011.

[21] H. Yoo and S.-K. Sul, "A novel approach to reduce line harmonic current for a three-phase diode rectifier-fed electrolytic capacitor-less inverter," in *Proc. Appl. Power Electron. Conf. Expo.*, Feb. 2009, pp. 1897–1903.

[22] H. Shin, H-.G. Choi, and J-.I. Ha, "DC-link shunt compensator for three-phase system with small DC-link capacitor," in *Proc. Int. Conf. Power Electron. ECCE Asia 2015*, Jun., pp. 33–39.

[23] X. Du, L. Zhou, H. Lu, and H.-M. Tai, "DC link active power filter for three-phase diode rectifier," *IEEE Trans. Ind. Electron.*, vol. 59, no. 3, pp. 1430–1442, Mar. 2012.

[24] P. Pejovic, P. Bozovic, and D. Shmilovitz, "Low-harmonic, three-phase rectifier that applies current injection and a passive resistance emulator," *IEEE Power Electron. Lett.*, vol. 3, no. 3, pp. 96–100, Sep. 2005.

[25] T. B. Soeiro and J. W. Kolar, "Analysis of high-efficiency three-phase two- and three-level unidirectional hybrid rectifiers," *IEEE Trans. Ind. Electron.*, vol. 60, no. 9, pp. 3589–3601, Sep. 2013.

[26] S. Rahmani, A. Hamadi, K. A.- Haddad, and L. A. Dessaint, "A combination of shunt hybrid power filter and thyristor-controlled reactor for power quality," *IEEE Trans. Ind. Electron.*, vol. 61, no. 5, pp. 2152–2164, May 2014.

[27] B. Choi and B.-H. Cho, "Intermediate line filter design to meet both impedance compatibility and EMI specification," *IEEE Trans. Power Electron.*, vol. 10, no. 5, pp. 583–588, Sep. 1995.

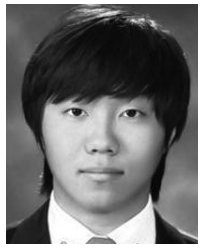

Hojoon Shin (S'12) received the B.S. degree in electronic and electrical engineering from Kyungpook National University, Daegu, Korea, in 2009, and the M.S. and Ph.D. degrees in electrical engineering and computer science from Seoul National University, Seoul, Korea, in 2011 and 2015, respectively.

He is currently a Researcher in Hyundai Motor Company. His current research interests include electric vehicles and renewable energy power conversion systems.

Yeongrack Son (S'13) was born in Korea in 1988. He received the B.S. and M.S. degrees in electrical engineering from Seoul National University, Seoul, Korea, in 2011 and 2013, respectively, where he is currently working toward the Ph.D. degree.

His current research interests include low-cost electric machine drives and the driving structure of the hybrid electric vehicle (HEV).

Jung-Ik Ha (S'97–M'01–SM'12) was born in Korea in 1971. He received the B.S., M.S., and Ph.D. degrees in electrical engineering from Seoul National University, Seoul, Korea, in 1995, 1997, and 2001, respectively.

From 2001 to 2002, he was a Researcher in Yaskawa Electric Co., Japan. From 2003 to 2008, he was with Samsung Electronics Co., Korea, as a Senior and Principal Engineer. From 2009 to 2010, he was a Chief Technology Officer with LS Mechapion Co., Korea. Since 2010, he has been with the Department of Electrical and Computer Engineering at Seoul National University, Korea, where he is now an Associate Professor. His current research interests include circuits and control in high efficiency and integrated electric energy conversions for various industrial fields.